



HAL
open science

Modal parameters and damage evaluation of steel fiber reinforced concrete under flexural cyclic loadings

Iranildo Barbosa Da Silva Junior, Cássio Marques Rodrigues Gaspar, Vitor Moreira de Alencar Monteiro, Flávio de Andrade Silva

► To cite this version:

Iranildo Barbosa Da Silva Junior, Cássio Marques Rodrigues Gaspar, Vitor Moreira de Alencar Monteiro, Flávio de Andrade Silva. Modal parameters and damage evaluation of steel fiber reinforced concrete under flexural cyclic loadings. *Journal of Building Engineering*, 2024, 97, pp.110797. 10.1016/j.jobbe.2024.110797 . hal-04707418

HAL Id: hal-04707418

<https://hal.science/hal-04707418v1>

Submitted on 4 Oct 2024

HAL is a multi-disciplinary open access archive for the deposit and dissemination of scientific research documents, whether they are published or not. The documents may come from teaching and research institutions in France or abroad, or from public or private research centers.

L'archive ouverte pluridisciplinaire **HAL**, est destinée au dépôt et à la diffusion de documents scientifiques de niveau recherche, publiés ou non, émanant des établissements d'enseignement et de recherche français ou étrangers, des laboratoires publics ou privés.

Submitted version

**Modal parameters and damage evaluation of steel fiber reinforced concrete under
flexural cyclic loadings**

Iranildo Barbosa da Silva Junior, Cássio Marques Rodrigues Gaspar, Vitor Moreira de Alencar
Monteiro and Flávio de Andrade Silva

Department of Civil and Environmental Engineering, Pontificia Universidade Católica
do Rio de Janeiro (PUC-Rio), Rua Marques de São Vicente 225, 22451-900 - Rio de
Janeiro - RJ, Brazil.

July 2024

Abstract

Structures may be subjected to static and dynamic loads during their service life. When it comes to the dynamic spectrum, wind action, ocean waves and seismic loads are key examples and are responsible for cracking evolution and material degradation along the time. Therefore, the fatigue behavior of cementitious materials has been receiving great attention due to cyclic loading that can be of natural occurrence or induced by human activity lately. The present research aims to investigate the evolution of the modal parameters of steel fiber reinforced concretes under flexural cyclic load and to evaluate how the mechanical degradation can be monitored from a non-destructive impact modal testing over the cycles. Cyclic tests were conducted in the material level on pre-cracked prisms. A self-consolidating 60 MPa concrete with hooked-ends steel fibers was developed for this study. Fatigue tests were carried on a continuous loading frequency throughout the cycles with a stress ratio of 0.3 and a stress level of 80%. The material's dynamic properties, including natural frequencies, vibration modes and damping ratios, were tracked to assess the level of damage using modal testing techniques. It was possible to identify the damage level with the variation of natural frequencies, vibration modes and damping. The Modal Assurance Criterion (MAC) analyses were used to evaluate the sensitivity of damage in the mode shapes. The stiffness degradation showed to be approximately higher than the resulting damage obtained with dynamic test and the first flexural mode and the following fifth and sixth vibration modes were more affected along the cycles. The evolution of damping ratios throughout the cycles showed to be more sensitive to damage during the fatigue life.

Keywords

Cyclic test, Fiber reinforced concrete, Mechanical degradation, Non-destructive testing, Dynamic testing.

1 Introduction

The careful analysis of the structural dynamic response is key when it comes to the study of the concrete response under distinct cyclic loads, such as wind action, ocean waves and seismic activity [1]. Considering that many structures are exposed to cyclic loads, researchers and designers must account for the effects of repeated loading to prevent structural fatigue failure [1–3]. Even if fatigue collapse does not occur, cyclic loading can negatively impact material properties such as strength, toughness, stiffness, and durability under service conditions [4–8].

To extend the service life of structures and facilitate rehabilitation, alternative methods such as the use of steel fibers as reinforcement have been employed. Concrete is inherently brittle with low strain capacity and tensile strength. However, the addition of fibers can significantly enhance its resistance to tensile stresses [9,10] and, consequently, modify its brittle behavior [11]. Steel fiber-reinforced concrete (SFRC) offers increased durability, crack control, ductility, toughness, and strength, making it a reliable construction material for various applications [12–14]. It should be noted that the addition of fibers is typically limited to around 1% of the concrete volume, as higher percentages can reduce workability and affect the effectiveness of fibers in the concrete [11,15].

Fatigue failure in concrete is attributed to the gradual accumulation of microcracks and the loss of stiffness over time [1,16]. Each cycle of cyclic loading causes residual strain, resulting in permanent and progressive structural changes within the material [14]. The critical analysis of damage evolution is crucial for estimating the decrease in concrete performance along the cycles and in predicting fatigue life in structures subjected to repeated loads [11].

The interest in monitoring and detecting damage in structures early on is a frequent concern in civil engineering. Various methods, such as acoustic [18], ultrasonic [19], magnetic [20], and thermal field techniques [21], are used for localized damage detection. However, the need for global, quantitative methods led to research on vibration-based damage detection. Research in this field has been driven by high-profile failures, economic factors, technical advancements, and aging infrastructure issues [21]. Technological progress in computing, sensors, and finite element methods has enhanced vibration-based damage detection.

In civil engineering, non-destructive vibration-based damage detection and monitoring methods have been widely used to assess the level of damage in materials and structures

[22]. Initially developed in aerospace and mechanical engineering, these techniques have gained significant attention in bridge structures since the early 1980s [23]. These methods rely on vibration sensor data, which is utilized to estimate dynamic and modal parameters through frequency response function (FRF) analysis [23–25]. By comparing the vibration modes and natural frequencies of undamaged and damaged materials, algorithms can identify damage information such as location and magnitude. One such method involves modal testing via Experimental Modal Analysis (EMA) using either an impact hammer [24,26] or electrodynamic shaker [55]. For large civil structures subjected to ambient forces, the Operational Modal Analysis (OMA) approach has attracted interest because it requires only measurements of the dynamic response of the structure under operational conditions (usually measured by accelerometers), rather than controlled and measurable excitation as in the EMA approach [54]. Both EMA and OMA approaches can be used as tools to analyze the correlation between experimental data and various damage levels to evaluate the dynamic properties of the material or structure.

When concrete undergoes damage, its mechanical properties, such as stiffness and damping, are directly affected, subsequently influencing the modal characteristics of the structural system, including natural frequencies, vibration modes, and damping ratios [25]. This relationship has led to the development of several vibration-based damage detection techniques based on stiffness [21,25–27], damping [26,28,29], modal shapes [30–32], natural frequencies [31,33–35], or FRF [23,25].

The study conducted by Salawu [36] on damage detection in structures using changes in modal parameters offers the possibility of using data from dynamic test for identifying, locating, and quantifying damage. Results of tests conducted at different times offer the opportunity of monitoring changes in structural condition with time. However, Salawu [36] also acknowledges that this process is complex, cites others factors to consider as the crack length, damage location, the effect of ambient conditions on the dynamic response of the structure and the consistency and reliability of the testing procedures that must be overcome in future works in this field.

Modena et al. [33] proposed that the utilization of higher modes was more accurate to localize damage than the lowers, highlighting the sensitivity of these modes. Zhao et al. [31], in turn, verified that the variation in natural frequencies and mode shapes can be employed for damage localization and quantification, emphasizing the use of Modal Assurance Criterion (MAC) to analyze mode shapes sensitivity to damage. Furthermore, Limongelli [23] introduced an innovative approach by considering the Frequency

Response Function (FRF) and its spline interpolation as a basis for damage detection. Zhan et al. [37] also adopted the FRF as a damage index, demonstrating the diverse number of methodologies to detect damage in structures.

The Impact Hammer test, which involves using a hammer as an input sensor and accelerometers as output sensors, has proven to be an accurate and cost-effective approach to damage monitoring and detection [24, 25]. Therefore, modal testing can establish a strong correlation between experimental mechanical data and different damage levels in SFRC structures.

The objective of this work is to develop a non-destructive methodology for estimating the damage level of steel-fiber-reinforced concrete during flexural fatigue tests by analyzing the material's vibration response to external excitation. The impact hammer test method is employed to estimate dynamic properties based on the vibration response of the SFRC material. The flexural fatigue tests were performed on notched pre-cracked prisms in accordance with EN 14651 standard [41]. A self-consolidating 60 MPa concrete with hooked-ends steel fibers with volume fraction of 40 kg/m³ was used for this study. The fatigue tests were performed under stress level of 80%, stress ratio of 0.3 and loading frequency of 6 Hz. The alteration of dynamic parameters (natural frequency, damping, and vibration modes) is used to determine the damage level based on the variation of mechanical parameters (stiffness and energy dissipation) during the cyclic test.

2 Experimental program

2.1 Material properties

The concrete specimens were manufactured using the following cementitious materials: the Portland cement was the Brazilian type CPII F-32, fly ash, silica fume and silica flour. Sand river was used with density around 2.7 g/m³, with two particle size: the first ranging from 0.15 mm to 0.85 mm and the second ranging from 0.85 mm to 4.80 mm and coarse aggregate with maximum diameter of 9.5 mm. To provide the necessary workability (650 mm of slump flow), the superplasticizer MasterGlenium 51 (29% of solid content) was used and the viscosity modifying admixture MasterMatrix VMA 358. The proportion of superplasticizer was set to 5.5% of the mass of the cement. The fresh concrete mixtures were characterized according to their flow ability in accordance with ASTM C1611 standard [38]. The assessment of the self-consolidating concrete spread was performed by the average of three perpendicular measurements SCC mass diameters [39]. Although a high amount of superplasticizer was used, the matrix did not present neither visible

segregation nor excessive porosity. Steel fibers with hooked-ends were used as reinforcement.

The steel fiber presents a length (L) of 35 mm, diameter (d) of 0.55 mm, aspect ratio of 65 (L/d) and the fiber volume fractions used were 40 kg/m³. With a water/cement ratio of 0.50, the resulting matrix presented specific compressive strength of 60 ± 3 MPa at 28 days. The complete mix composition for the present research can be verified in Table 1. More information on the applied self-consolidating concrete (SCC) is available at the work of Cardoso et al. [40].

Table 1 - Mix composition of matrix and steel fiber reinforced self-consolidating concrete.

Constituent	Mixture
Coarse aggregate (kg/m ³)	465.04
Sand (S1)* (kg/m ³)	826.76
Sand (S2)* (kg/m ³)	99.60
Silica Mesh 325 (kg/m ³)	70
Cement (kg/m ³)	360
Fly Ash (kg/m ³)	168
Silica Fume (kg/m ³)	45
Water (kg/m ³)	164 (6%)
Superplasticizer (%)	5.5
Viscosity modifying admixture (%)	0.75
Hooked end fiber (kg/m ³)	40
w/c ratio	0.50

*Sand (S1) with diameter ranging from (0.15<A1<0.85 mm) and Sand (S2) with diameter ranging from (0.85<A2<4.80).

2.2 Mixing procedure

The complete mixing procedure can be divided in five main stages. The aggregates (river sands S1 and S2, and coarse aggregate) are first added inside the mixer with 60% of the water and blended for at least 1 min. Thereafter, the mineral and cementitious materials (fly ash, silica fume and silica flour) are mixed with the aggregates for 1 min. Afterwards, the cement is added and blended for another 1 min. The remaining water (40%), the

superplasticizer and the viscosity modifying admixture is blended with the rest of the materials for at least 20 min. For the final stage, the steel fibers are added gradually to the concrete matrix and blended for 5 min. All specimens were then cured at saturated conditions and at room temperature of 25 °C before testing until 28 days of curing.

3 Tests procedures

3.1. Monotonic three-point bending test

The steel fiber reinforced self-consolidating concrete was characterized through three-point bending tests following the EN 14651 [41] standard. A total of three specimens were manufactured and subjected to monotonic testing. Each specimen had a cross-section measuring 150 mm × 150 mm and a length of 550 mm, and pre-notched at mid-span, creating a notch with dimensions of 25 mm depth and 3 mm width. The loading device was positioned between the supports at the middle span of the specimens, with a span of 500 mm.

The tests were conducted after a curing period of 28 days. All three-point bending tests were carried on closed-loop control system, employing an MTS servo-controlled hydraulic testing machine. A load cell with a capacity of 100 kN was attached to the piston. The tests were controlled by monitoring the crack mouth opening displacement (CMOD) using a clip gauge device at a rate of 0.05 mm/min until it reached 0.10 mm. Subsequently, the test was continued at a rate of 0.20 mm/min of CMOD until reaching 4 mm, which indicated specimen failure.

3.2 Cyclic bending test

To evaluate the cyclic behavior and damage evolution of steel fiber reinforced self-consolidating concretes, 5 prisms were tested under cyclic flexural load. The cyclic test was divided into 3 main stages (see Figure 1):

1. The initial pre-cracking static stage starts controlled by the crack mouth opening displacement at a 0.05 mm/min rate until reaching 0.10 mm of CMOD and then 0.2 mm/min rate up to the CMOD of 0.5 mm.
2. The second stage occurs the unloading of the specimen with rate of 5 kN/min until the load reach zero. The flexural residual strength ($f_{R,1}$) is computed at 0.5 mm of crack mouth opening displacement – CMOD.

- The third stage occurs the cyclic test: defined the maximum and minimum loads, cyclic test started by loading the sample up to P_{med} , corresponding to the mean between P_{upp} and P_{low} . After that, was applied a load-controlled and a sinusoidal wave of frequency of 6 Hz on pre-cracked specimens. The tests were subjected to a continuous loading frequency throughout the cycles with a stress ratio (P_{low}/P_{upp}) of 0.3 and a stress level (P_{upp}) of 80% of the $f_{R,I}$.

The test limit has set to end as soon as specimens reach failure (CMOD > 4 mm). Figure 1 illustrates the test protocol adopted for the cyclic tests. The cyclic tests were carried out after at least 28 days of curing of the specimens.

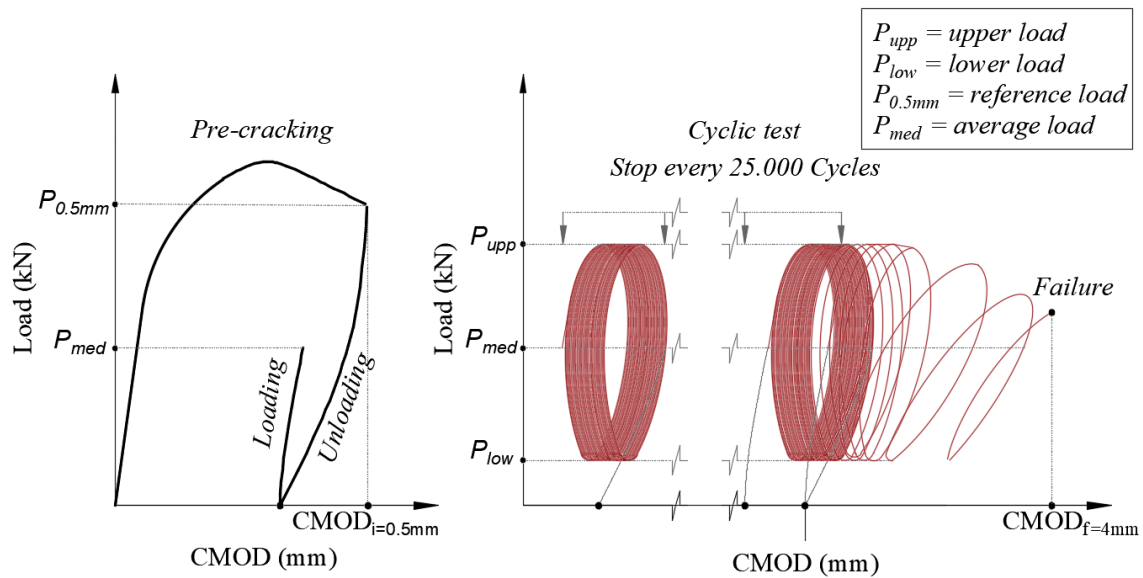


Figure 1: Overview of the cyclic bending test protocol adopted for the cyclic test.

3.3 Experimental dynamic test using impact hammer

The non-destructive dynamic test was divided into 3 stages (see Figure 2), namely: the initial stage when the material is intact, before the initial static pre-cracking, the second being the pre-cracking stage with a static test up to the CMOD of 0.5mm, and the third stage occurs during the cyclic test. The third stage consists of stopping the test every 25,000 cycles to measure the dynamic response with the impact hammer until reaching the material failure. A total of four specimens were subjected to non-destructive dynamic test.

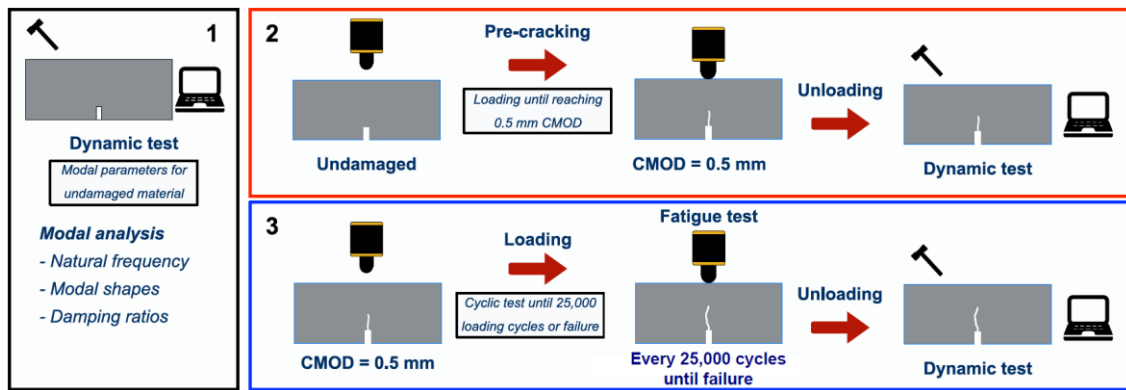


Figure 2: Overview of the dynamic test phases.

The impact hammer test was conducted to estimate the dynamic parameters in terms of natural frequencies, vibration modes and damping ratios of the fiber reinforced concrete throughout the cyclic test. Three accelerometers were installed on the specimen: one in the middle of the span, and the other two at 1/4 of the span length in the corners (see Figure 4). The signals from the hammer with the metallic tip and the uniaxial accelerometer used here (types PCB Piezotronics 086C03 and HBK 4533-B001, respectively) were acquired through the CompactDAQ USB-9162 acquisition system from National Instruments (NI), equipped with Integrated Electronic Piezoelectric (IEPE) analogue input modules (NI 9233).

The non-destructive tests were performed and processed using ARTeMIS software. The signals were recorded with a sampling frequency of 25000 Hz which is enough to capture natural frequencies until 12500 Hz according to the sampling theorem [42]. Thus, the relationship between the output (acceleration) and input (force) signals, in frequency domain, is defined as the Frequency Response Function (FRF) of the system [42]. The force pulse duration is 1.3 s used to measure the force signal. The general form of the force window is showed in Figure 3.a and acceleration over time in Figure 3.b.

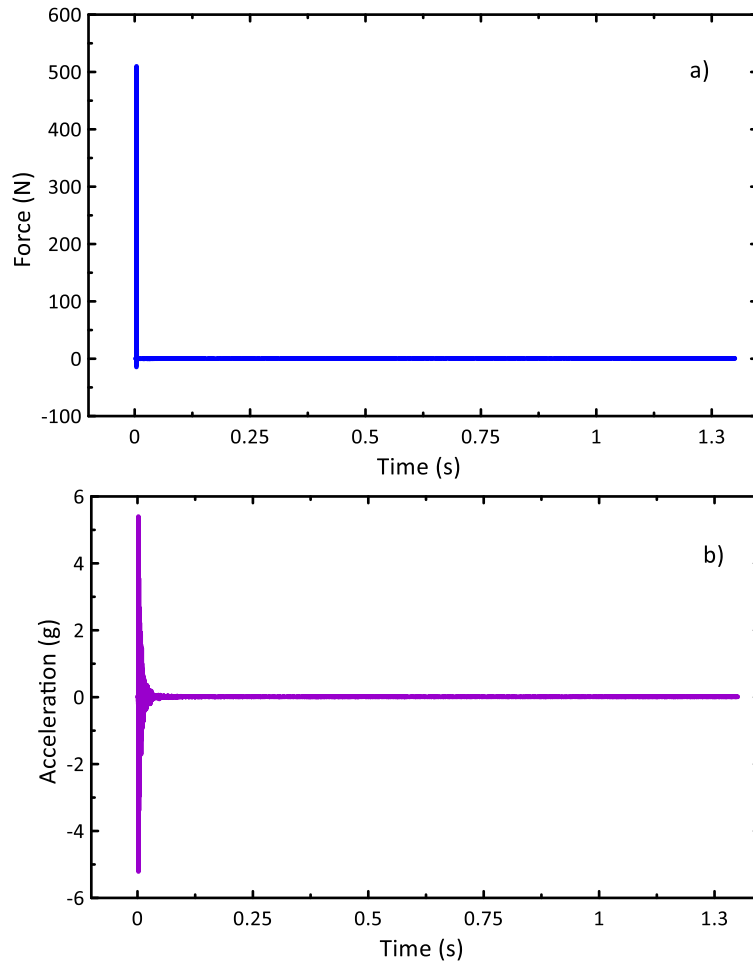


Figure 3: Response signal: (a) force and (b) acceleration magnitude obtain during the impact test.

The surface of the specimen was divided into 36 points every 50 mm and 75 mm in the longitudinal and transverse direction, respectively. Figure 4 shows the layout of the modal test and the position of the accelerometers on the material. In order to compute the 36 experimental average FRFs in one plot for each specimen (the total FRFs measurements is equal to $36 \times 3 = 108$, as each point was hit 3 times to obtain average values for signal processing purposes), the Complex Mode Indicator Function (CMIF) was used [27].

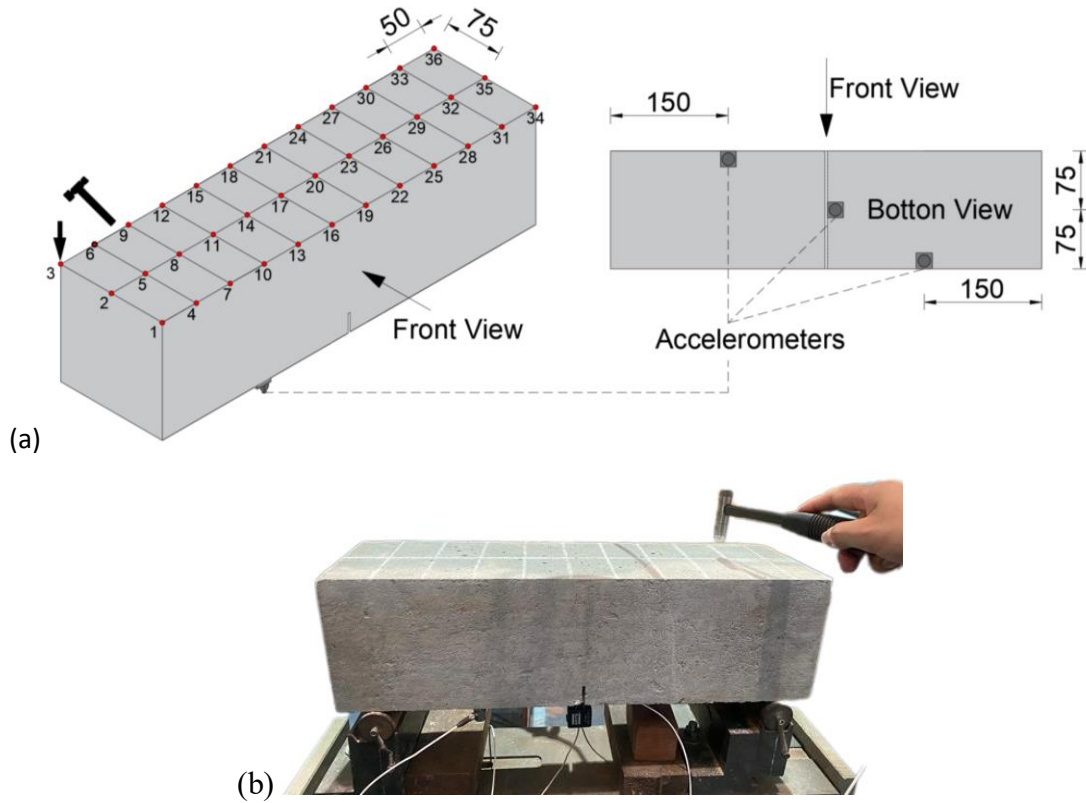


Figure 4: Dynamic test: (a) layout of the impact hammer test and uniaxial accelerometers positions (b) photo of setup during the test. Dimensions in mm.

3.4 Modal Correlation

An important tool to check if the identified vibration modes are consistent is established through the Modal Assurance Criteria (MAC). The MAC evaluates the degree of linearity between two different modal vectors (whether real or complex) which results in a scalar quantity varying from 0 to 1. This parameter is defined by Eq. (1).

$$MAC_{ij} = \frac{|\{\psi_i\}^T \{\psi_j^*\}|^2}{\{\psi_i\}^T \{\psi_i^*\} \{\psi_j\}^T \{\psi_j^*\}} \quad (1)$$

Where $\{\psi_i\}$ is the i^{th} mode shape of the undamaged structure and $\{\psi_j\}$ is the corresponding mode shape of the damaged structure. When the two sets of mode shapes fit each other well, the value is close to 1. Therefore, there is no obvious change in mode shape before and after the occurrence of damage. Meanwhile, a value of 0 means no correlation [31] and it can be interpreted that the mode shape is sensitive to the damage.

MAC values as above 0.9 (90%) can be considered well-correlated whereas values less than 0.1 (10%) can be classified as uncorrelated. Also, the boundaries 80% and 20%, respectively, are acceptable.

4 Results and Discussion

4.1 Mechanical degradation during fatigue tests

All three samples subject to monotonic bending test presented a deflection hardening behavior, as indicated by Figure 5. This behavior is attributed to the active influence of the bridging effect in controlling crack propagation and, consequently, enhancing the flexural strength of the concrete, which will vary according to the number of fibers acting on the cross section and their adherence to the matrix.

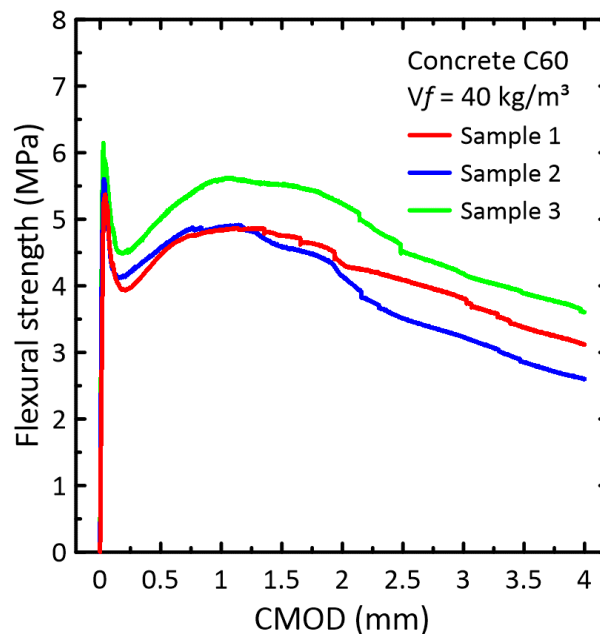


Figure 5: Flexural strength \times CMOD curve from three-point monotonic bending test.

The results of the tests are shown in Table 2 presenting the flexural parameters according to EN 14651 [41]. The concept of the limit of proportionality (P_{LOP} and σ_{LOP}) is employed to define the highest stress corresponding to the elastic behavior of the material. Similarly, the modulus of rupture (P_{MOR} and σ_{MOR}) is the maximum stress observed along the

flexural stress-CMOD curve from the three-point bending test. Also, the residual flexural ($f_{R,1}$, $f_{R,2}$, $f_{R,3}$, and $f_{R,4}$) stress is presented.

Table 2. Quasi-static flexural strength parameters results.

Sample	P_{LOP} (kN)	σ_{LOP} (MPa)	P_{MOR} (kN)	σ_{MOR} (MPa)	$f_{R,1}$ (MPa)	$f_{R,2}$ (MPa)	$f_{R,3}$ (MPa)	$f_{R,4}$ (MPa)
CP1	15.57	4.98	16.78	5.37	4.47	4.33	3.81	3.11
CP2	13.10	4.20	17.51	5.60	4.58	4.15	3.23	2.60
CP3	17.75	5.68	19.20	6.14	5.01	5.23	4.18	3.60
Average	15.47	4.95	17.83	5.70	4.69	4.57	3.74	3.10
Standard deviation	2.33	0.74	1.24	0.39	0.29	0.58	0.48	0.50

The cyclic bending test on pre-cracked concrete specimens is a methodology that applies percentages of actual resisted load of each specimen instead of using the mean results from flexural tests, which can reduce the scattering and providing concise information to the phase of the flexural test that the fibers are more effective (cracked state) [43]. Previous research showed the fatigue life is a result of probabilistic difference in fiber orientation and distribution and the scatter behavior of the fatigue itself [43]. The residual flexural strength is an important parameter to evaluate the cyclic behavior along the loading and unloading cycles. The composite post-peak strength is essentially controlled by the fibers bridging effect after matrix disruption [8].

Figure 6.a shows the flexural strength and the $f_{R,1}$ during the pre-crack phase and the evolution of the load and unloading cycles during the fatigue test. Figure 6.b shows the stiffness degradation over the cycles with the hysteretic cycles over the fatigue test. It can be seen a progressive stiffness decay that can be associated with crack opening development. Crack keeps growing up on the specimen notch until reaching a critical size and consequently the material failure. As can be seen, the cycles do not show higher crack opening range (Δ CMOD) during the beginning of the test and show a faster increase of Δ CMOD at the end of the cyclic test.

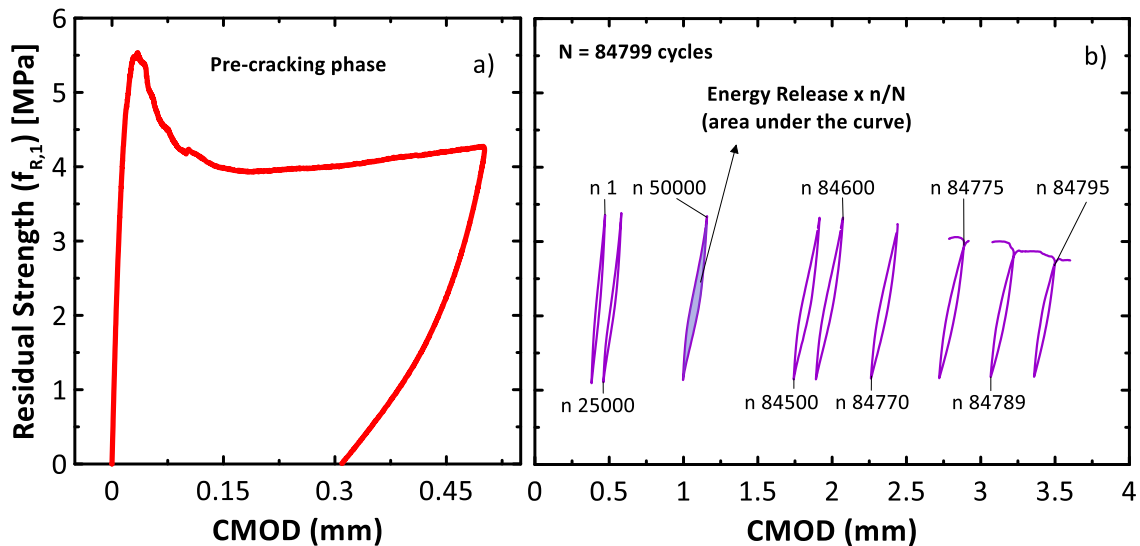


Figure 6: Flexural strength and $f_{R,I}$ during the pre-cracked stage (a) and residual strength (b) throughout the fatigue test.

The stiffness (k) is determined as the slope and the energy release (ER) is the area under each hysteresis loop at each cycle during the fatigue test. Figure 7 shows how these parameters were determined in this work. The initial stiffness (k_0) and initial energy release (ER_0) corresponds to the stiffness and energy release at the cycle number 100 of each test. The values of k_0 and ER_0 for all specimens are shown in Table 3.

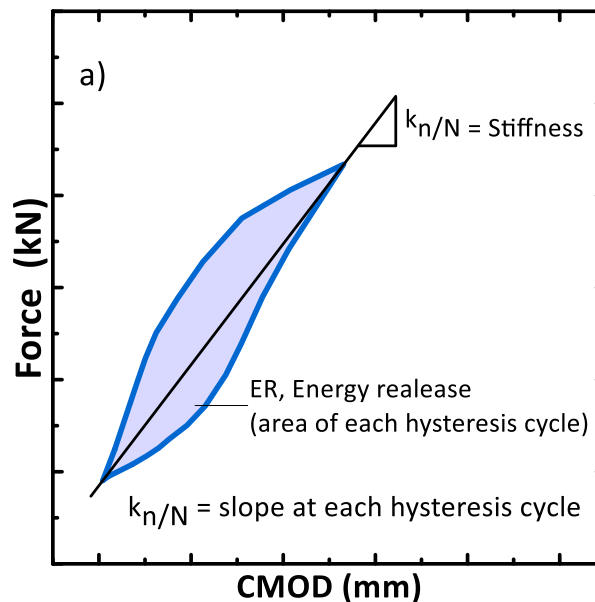


Figure 7: Example of stiffness calculation and energy release for the hysteresis loop at cycle i .

The fatigue life can be influenced by several parameters such as stress level, stress ratio, loading frequency, amplitude, loading sequence and material properties [47-49]. In general, a high number of cycles are achieved in fatigue experiments for fiber reinforced concrete, reaching 1.000.000 cycles depending on the load level (P_{upp}) [44]. In this research all evaluated samples failed before 200,000 cycles for the load level of 80% and stress ratio of 0.3. At high fatigue load levels (higher than 60%), this behavior can be attributed to the higher energy imposed on the specimens within a short time duration [44].

Since the crack has already taken place prior to the fatigue test, the composite post-peak strength is crucial for verifying the material stiffness during fatigue loading cycles. The stiffness and the energy release of the specimens are directly affected by the quantity of fiber bridging on the cracked concrete section. The greater number of fibers on the cracked concrete section is responsible for enhancing the post-peak resistance and, consequently, incrementing stiffness during the fatigue cycles and inhibit the energy release. Hence, it is possible to verify a linear correlation between the flexural residual strength at 0.50 mm of CMOD ($f_{R,1}$) and the initial stiffness (k_0) and energy release ER_0 . Figure 8 displays a linear correlation between k_0 and ER_0 with $f_{R,1}$. The linear correlation can also be verified in Eq. (2) and (3).

$$k_0 = 16.10f_{R,1} + 9.90; \quad R^2 = 0.98 \quad (2)$$

$$ER_0 = 0.0235f_{R,1} + 0.0079; \quad R^2 = 0.98 \quad (3)$$

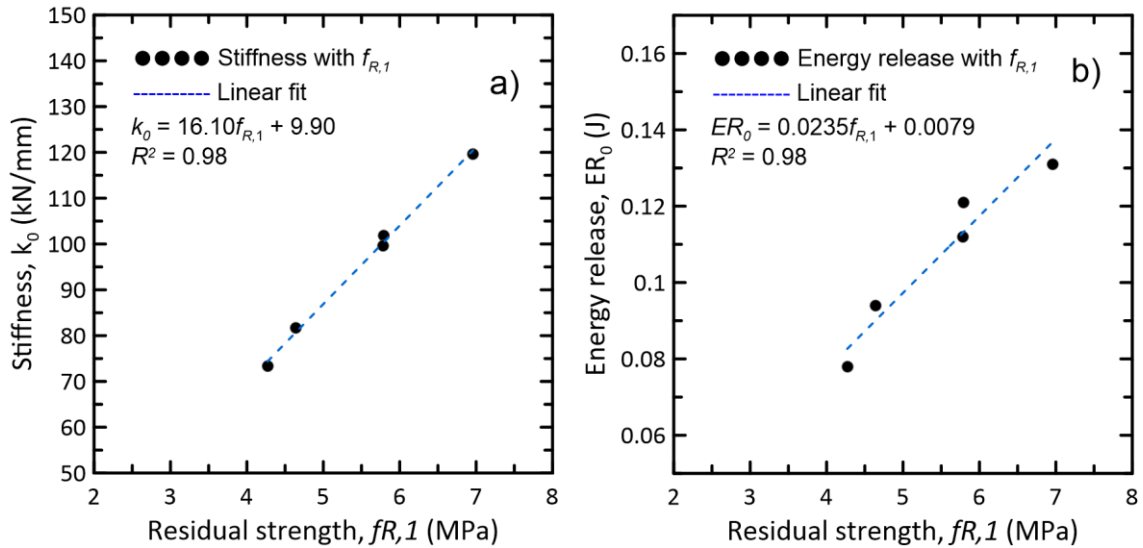


Figure 8: Linear correlation between stiffness (a) and energy release (b) with the residual strength ($f_{R,1}$) after the pre-cracking stage.

Figure 9.a reveals the progressive stiffness decay along the fatigue life of the material. To eliminate any influence of the initial stiffness, the stiffness is normalized with the k_0 associated as a Damage ratio (Figure 9.c). The decrease in stiffness is directly related to the crack evolution throughout the fatigue life of the specimen and is the main parameter to evaluate the mechanical degradation of the fiber reinforced concrete [45]. The S-shape curve is characterized by an initial deceleration stage followed by an almost linear second phase. When the specimen reaches its failure, the last stage of stiffness degradation is a sharp decrease [45].

Figure 9.b presents the evolution of the energy release over the fatigue life. The evolution of energy release normalized with E_0 is showed in Figure 9.d as energy release growth rate (ΔER). The variation of energy release showed distinct behavior in relation to stiffness evolution. First, the ΔER presents a linear behavior until reaching approximately $n/N = 0.80$. Subsequently, a sharp increase on the energy release takes place until reaching the fatigue failure. The slower rate of energy dissipation through time shows the capacity of SFRC to maintain its post-peak flexural stiffness along loading cycles and maintain the mechanical parameters through the fatigue life. The number of cycles until failure and the parameters used during the fatigue tests are shown in Table 3.

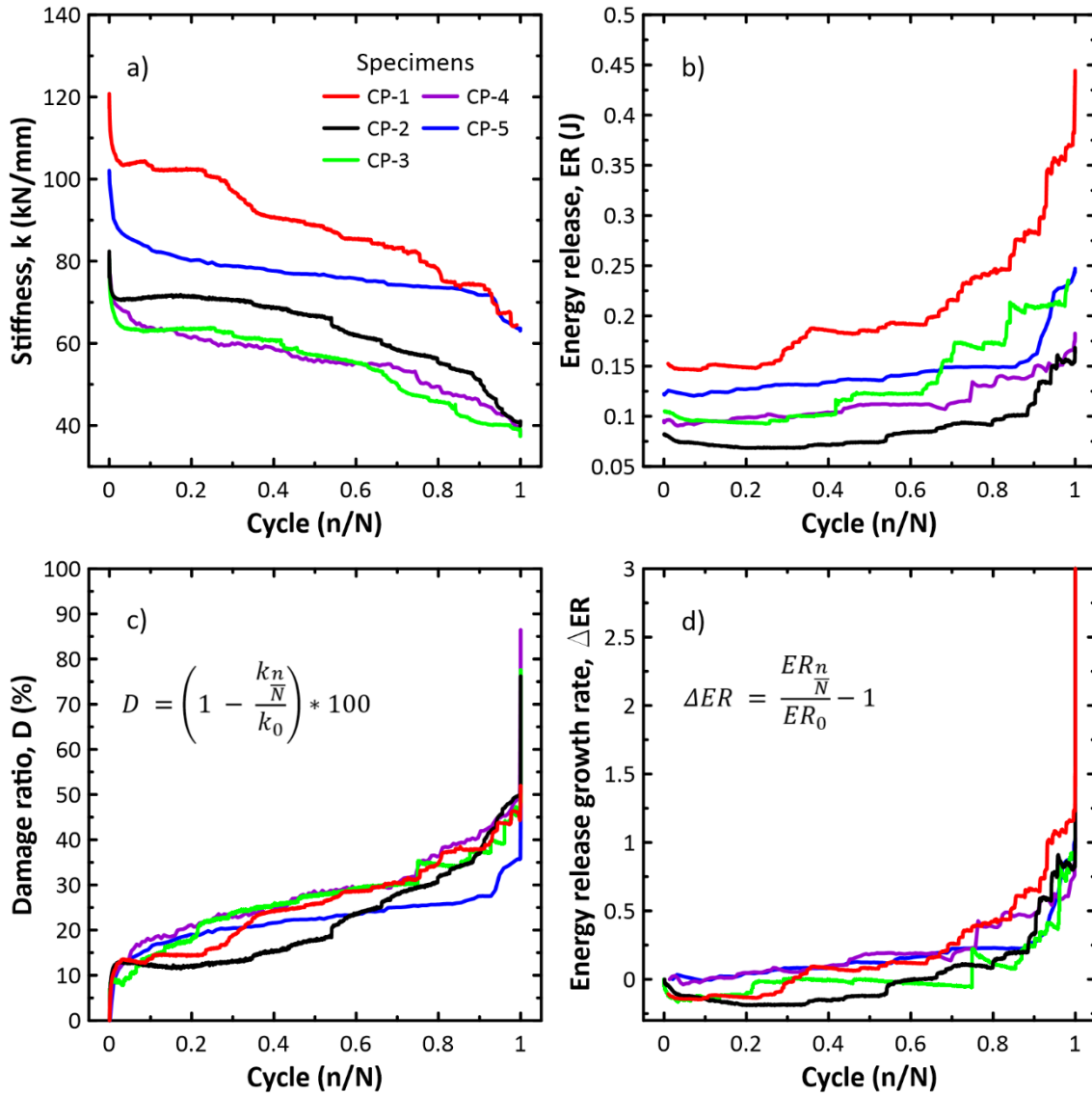


Figure 9: Mechanical deterioration of steel fiber reinforced self-consolidating concrete under stress level of 80% and stress ratio of 0.3: (a) stiffness decay, (b) energy release across n/N and (c) damage ratio and (d) energy release growth rate normalized over fatigue life.

Table 3: Cyclic bending tests results on pre-cracked steel fiber self-consolidating concrete specimens.

Sample	CP1	CP2	CP3	CP4	CP5
k_{elastic} (kN/mm)	1010.01	1295.61	1130.74	1052.52	921.62
E_{elastic} (J)	21.42	30.62	20.73	25.41	35.62
$P_{0.5\text{mm}}$ (kN)	21.75	21.24	13.34	14.32	14.49
$f_{R,1}$ (MPa)	6.96	5.79	4.27	5.78	4.64
Cycles until failure, N	84,799	82,104	59,337	26,995	134,566

CMOD _i (mm)	0.39	0.38	0.39	0.41	0.37
CMOD _f (mm)	4	4	4	4	4
ΔCMOD _i	3.61	3.59	3.61	3.61	3.6
k ₀ (kN/mm)	119.6	101.89	73.38	99.68	81.73
ER ₀ (J)	0.131	0.121	0.078	0.112	0.094

During the unloading and loading stage every 25,000 cycles the material presents an increase of damage that can be evaluated with the CMOD_i and CMOD_f (crack opening corresponding to the beginning and the end of the fatigue test, respectively). Figure 10.a shows the evolution of CMOD over the fatigue cycles. As can be seen, a similar progression for all samples with a three-stage trend: the first one is a constant growth of crack opening and a decreasing rate of CMOD evolution; the second stage is caused by a slow and gradual increase of damage, resulting in an almost linear CMOD per cycle; the third stage occurs just before failure, with sudden crack growth and a decrease in stiffness. Figure 10.b presents the CMOD evolution through relative load cycles number. The values of CMOD at each stage are shown in Table 4 until reaching failure (4 mm). After every loading stage, the material presented a slight increase of CMOD that shortened the fatigue life when compared to the continuous fatigue test (without the loading and unloading stops) where the material presents a slow and gradually increase of damage, resulting in an approximately linear CMOD per cycle regime [44].

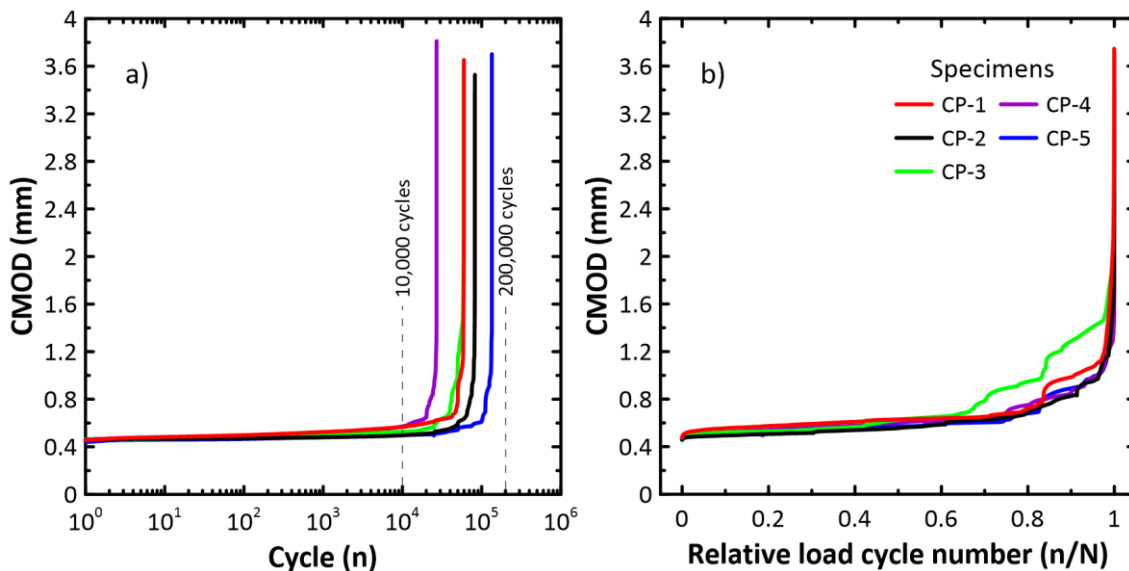


Figure 10: CMOD evolution for all tested specimens in accordance with (a) number of cycles (n) and (b) relative load cycles number (n/N).

Table 4: Results of reached CMOD after every loading and unloading stage.

Specimen		CP1	CP2	CP3	CP4	CP5	
Cycles (n)	0	CMODi	0.39	0.38	0.39	0.41	0.37
	25,000	CMODf	0.61	0.52	0.57	0.85	0.51
	25,000	CMODi	0.52	0.44	0.5	0.76	0.43
	50,000	CMODf	0.79	0.59	1.06	Failure	0.54
	75,000	CMODi	0.93	0.5	0.94	-	0.46
		CMODf	Failure	0.84	Failure	-	0.58
	100,000	CMODi	-	0.72	-	-	0.49
		CMODf	-	Failure	-	-	0.61
	125,000	CMODi	-	-	-	-	0.52
		CMODf	-	-	-	-	0.9
	150,000	CMODi	-	-	-	-	0.79
		CMODf	-	-	-	-	Failure

4.2 Damage evaluation through non-destructive dynamic testing

The Rational Fraction Polynomial in the Z domain method (RFP-Z) was applied to identify the experimental vibration modes in the vertical direction through the stabilization diagram processed in ARTEMIS software [50]. To evaluate the degradation of the modal parameters of fiber reinforced concrete, the impact hammer test was carried out on an undamaged sample to determine the initial parameters for comparison and over the fatigue test with incident of damage. Figure 11 shows the CMIF corresponding to the undamaged and damaged material for each stage over the cyclic test. To evaluate damage, an analysis will be conducted on the behavior of sample 1 (CP1) to enhance the understanding of the material's dynamic properties and evolution. The damage analysis will specifically examine the impact on the initial six vibration modes. The values presented in the tables will include data from all samples evaluated in this study.

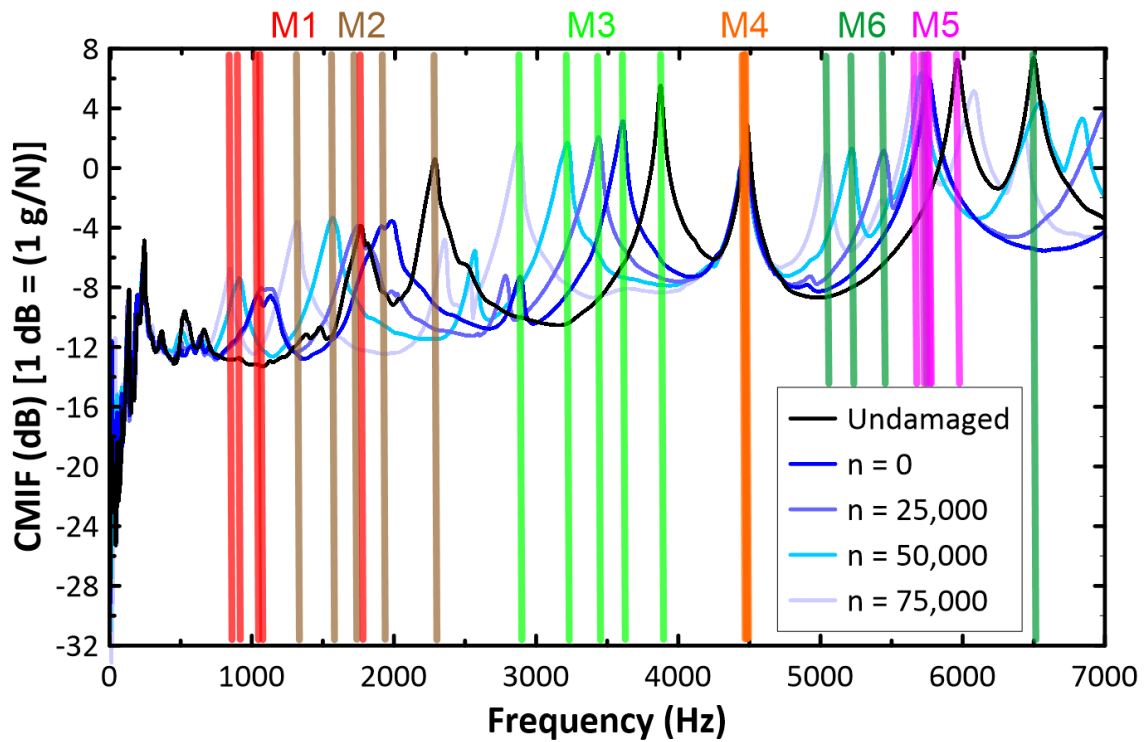


Figure 11: The Complex Mode Indicator Function (CMIF) computes the FRFs. The vertical lines indicate the identified six modes and its variation throughout the fatigue test.

With the aid of CMIF it was possible to obtain the vibration modes for each completed measurement. The peaks presented in the graph are identified during the post-processing stage and subsequently classified into stable and unstable using the FRP-Z function. The peaks identified as stable represent a vibration mode and exhibit damping. Figure 11 presented a clear trend where the stable peaks shift to the left as damage increases. This pattern will be further examined in the next section. The results in terms of natural frequencies and damping ratios for the undamaged phase are shown in Table 5 and the damaged phase with CMOD equals to 0.5 mm in Table 6.

4.2.1 Damage identification using frequency changes

When the material was subjected to damage after pre-cracking, it showed a great drop of 91% in stiffness in average for all samples (see Table 3 and 4). During the fatigue test, the reduction in stiffness was more gradual (see Figure 9.a). Consequently, it affected the natural frequency as this parameter is proportional to the stiffness. It is assumed that the

modal mass remains constant during cyclic loading, allowing a reduction in frequency to be correlated with a decrease in stiffness. Table 5 and 6 presents the average of natural frequencies and damping ratios for all samples for the undamaged and after pre-cracking stage, respectively.

Table 5: Average of identified experimental natural frequencies and damping ratios and coefficient of variation for all samples for the undamaged material. Standard deviation in parenthesis.

Mode	Experimental model				Modal behavior
	Frequency (Hz)	Coefficient of variation, CV (%)	Damping ratio (%)	CV (%)	
1	1716.88 (103.78)	6.04%	2.10 (0.53)	25.19%	1 st flexural
2	2285.60 (70.59)	3.09%	1.34 (0.34)	25.55%	1st torsional
3	3930.04 (79.56)	2.02%	0.85 (0.47)	55.08%	2nd flexural
4	4485.07 (84.37)	1.88%	1.07 (1.15)	106.87%	2nd torsional
5	6047.50 (85.75)	1.42%	0.41 (0.04)	8.83%	3rd flexural
6	6562.50 (97.15)	1.48%	0.39 (0.04)	9.56%	3rd torsional

Table 6: Average of identified experimental natural frequencies and damping ratios and coefficient of variation for all samples for the CMOD equals to 0.5 mm phase. Standard deviation in parenthesis.

Mode	Experimental model				Modal behavior
	Frequency (Hz)	CV (%)	Damping ratio (%)	CV (%)	
1	1079.68 (67.83)	6.28%	5.15 (0.77)	14.86%	1 st flexural
2	1912.32 (7.89)	0.41%	2.94 (0.20)	6.88%	1st torsional
3	3613.76 (59.16)	1.64%	1.42 (0.39)	27.36%	2nd flexural
4	4490.37 (81.88)	1.82%	1.09 (0.93)	85.39%	2nd torsional
5	5864.09 (76.36)	1.30%	0.53 (0.06)	11.24%	3rd flexural
6	5640.98	1.04 %	0.80	34.10 %	3rd torsional

Examining the frequency response in Figure 11, becomes apparent that the lower modes exhibited close-spaced peaks for the damage cases, making it challenging to identify the

vibration mode accurately. On the other hand, the higher modes showed sharper peaks, facilitating damage detection.

Assuming a uniform behavior for all specimens during the dynamic test, Table 7 exhibits the natural frequencies for CP1 across all six modes throughout each stage, illustrating their evolution. Δ_{freq} is calculated by referencing the natural frequency from the undamaged phase and comparing it with the current frequency value of the analyzed phase. The reduction in structural stiffness due to a decrease in material frequency was observed throughout the test over the cyclic loading (see Table 7). Notably, the frequency of each mode exhibited a decreasing trend along the fatigue cycles, with one exception: the fourth mode (equivalent to the second torsional mode) maintained a constant frequency value throughout all cycles (see Figure 11).

Furthermore, after the pre-cracked stage, the sixth mode experienced a decrease in natural frequency, shifting to the left before the fifth mode (see Figure 11). This change in frequency indicates the severity of damage-induced alterations in the material's structural properties.

Table 7: Identified experimental natural frequencies for all stages and its evolution.

Modal Shape		M1	M2	M3	M4	M5	M6
Undamaged	Frequency	1767.755	2278.851	3870.968	4479.81	5963.05	6494.92
	n = 0	1043.896	1923.207	3574.696	4462.788	5760.075	5655.74
(CMOD = 0.5 mm)	Δ_{freq}	-41%	-16%	-8%	0%	-3%	-13%
	n = 25,000	1069.683	1738.278	3352.53	4458.398	5749.147	5400.84
n = 50,000	Δ_{freq}	-39%	-24%	-13%	0%	-4%	-17%
	Frequency	897.696	1546.715	3191.14	4457.999	5701.803	5196.14
n = 75,000	Δ_{freq}	-49%	-32%	-18%	0%	-4%	-20%
	Frequency	818.98	1285.68	2843.304	4455.65	5647.833	5023.56
	Δ_{freq}	-54%	-44%	-27%	-1%	-5%	-23%

Figure 12 shows the evolution of mechanical stiffness of CP1 and evolution of natural frequency during every stage. During the conducted tests, Figure 12.a demonstrated a decline in natural frequency after pre-cracking. Specifically, for the first flexural mode (represented by triangle markers), the frequency experienced a 41% reduction, while the first torsional mode saw a 16% decrease (dot markers), and the fourth mode remained nearly unchanged at all damage levels. The sixth mode showed a 13% reduction in

frequency. Figure 12.b shows the evolution of stiffness and natural frequency during the cyclic test. Accordingly, it can be summarized that the first mode closely followed the stiffness reduction, the second mode doesn't align with the reference curve but indicates a wider range of stiffness reduction among cycles; modes 3 and 6 are less sensitive but still show a decreasing trend; and finally, modes 4 and 5 are insensitive to damage. Therefore, this index proves capable of indicating the presence of damage. The reduction in stiffness caused a decrease in the frequency of the material by up to 54%, 27% and 5% for the first, second and third flexural modes, respectively and 44%, 1% and 23% for the first, second and third torsional modes, respectively, at the end of the fatigue life.

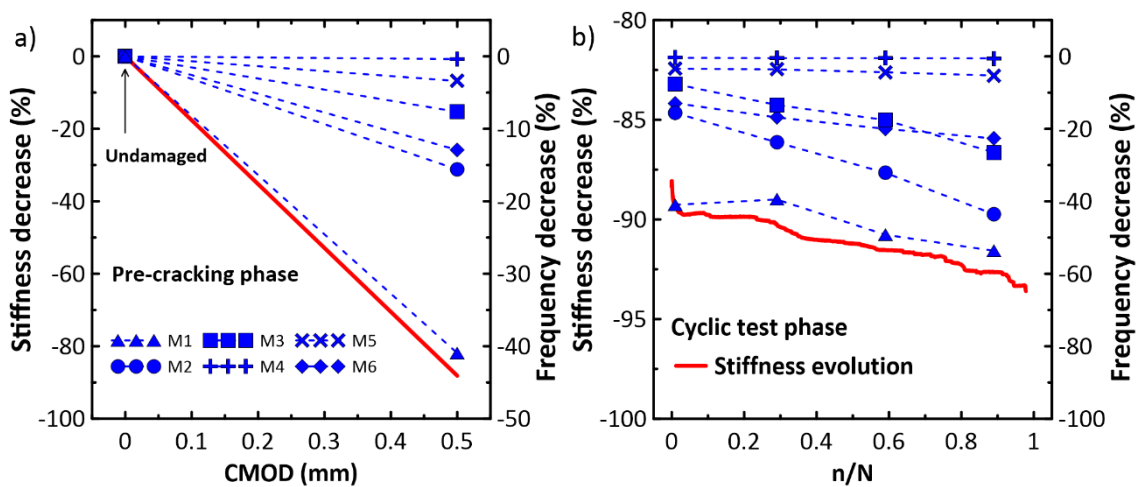


Figure 12: Stiffness (a) and stiffness versus frequency (b) variation for the six obtained modes for the sample 1 (CP1).

Figure 13 shows a comparison of the stiffness evolution and the evolution of the first vibration mode for all specimens analyzed in this work. In Figure 13.a, the variation of natural frequency is depicted, revealing a positive correlation during the pre-crack stage for the first flexural mode. Furthermore, Figure 13.b and Figure 13.c illustrate the evolution of stiffness and the variation of the first flexural mode for all specimens, respectively.

As shown in Figure 13.b, all specimens have a similar behavior during the fatigue life: a rapid decrease of stiffness after the initial cycles and a slow and gradual decrease of stiffness afterward, resulting in an approximately linear stiffness per cycle regime. A drastic decrease of stiffness occurs just before failure. Figure 13.c displays the evolution of natural frequency, showing a tendency for the specimens to follow the behavior of stiffness evolution, as observed in Figure 13.b.

Figure 13.c provided insights into the natural frequency evolution during the fatigue test, exhibiting a continuous decrease in stiffness throughout the cycles. Notably, the first flexural mode proved to be more representative of the global behavior in all stages, as anticipated due to the crack's progressive growth in the cross section, and its relevance to a flexural bending test. As the crack is in a region of high curvature for the first flexural mode, the reduction of frequency is showed to be more important [36].

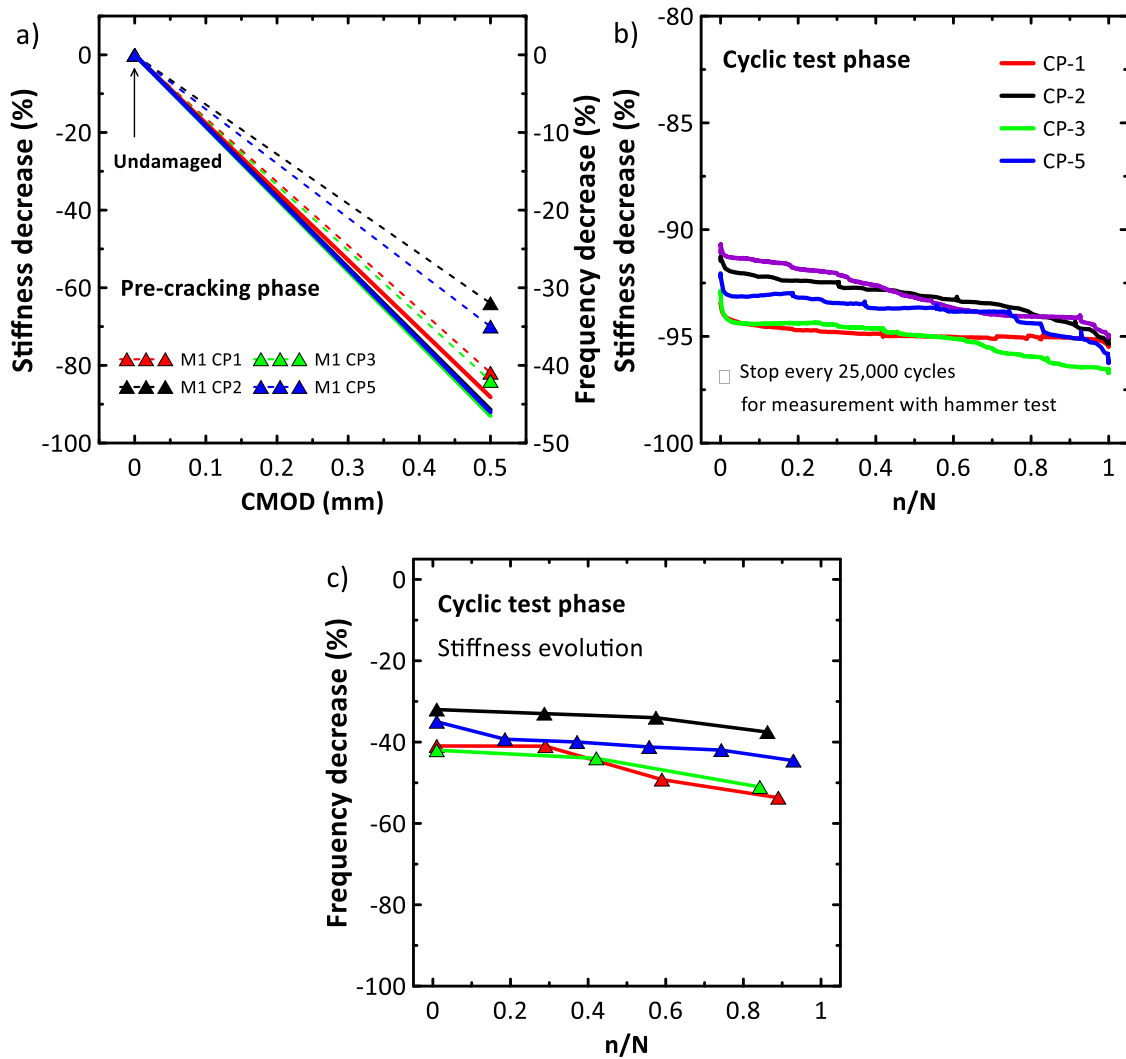


Figure 13: Evolution of the mechanical and modal parameters. (a) Stiffness and frequency decrease for the uncracked state and the pre-cracking stage, (b) evolution of stiffness and (c) decrease of natural frequency during the fatigue life.

4.2.2 Damage identification using vibration modes

During fatigue, the occurrence of damage induces changes in the material's stiffness, leading to modifications in modal properties, including mode shapes. These alterations can be effectively detected using the Modal Assurance Criteria (MAC), as indicated in section 3.4, enabling the evaluation of damage from the vibration modes. Figure 14 illustrate the evolution of six vibration modes obtained for each stage for specimen 1 (CP1), as all specimens behave comparably to each other. As can be seen, the first, third, and fifth modes (flexural modes) and the second, fourth, and sixth modes (torsional modes) are presented, along with their variations from the undamaged counterparts. By analyzing the MAC values (as seen in Figures 14 and 15), it becomes possible to determine the correlation between the undamaged and damaged material.

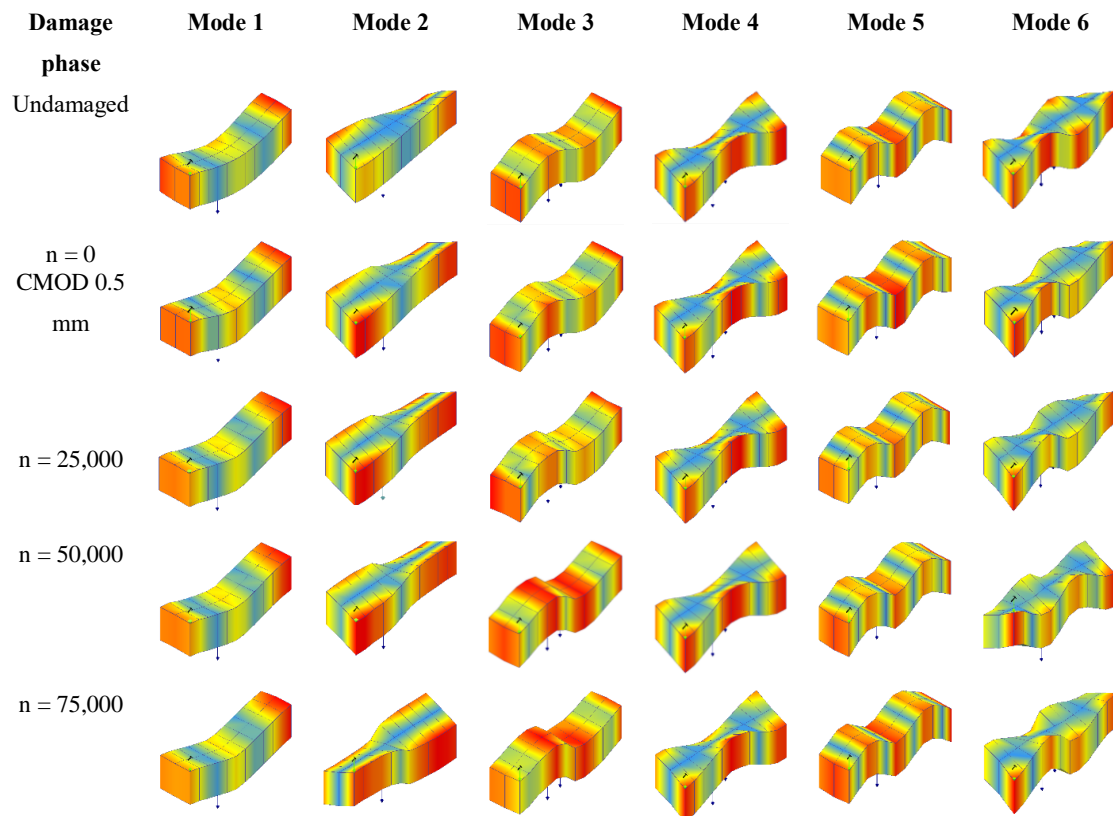


Figure 14: Vibration modes in vertical direction obtained over the impact hammer modal test for specimen 1 (CP1).

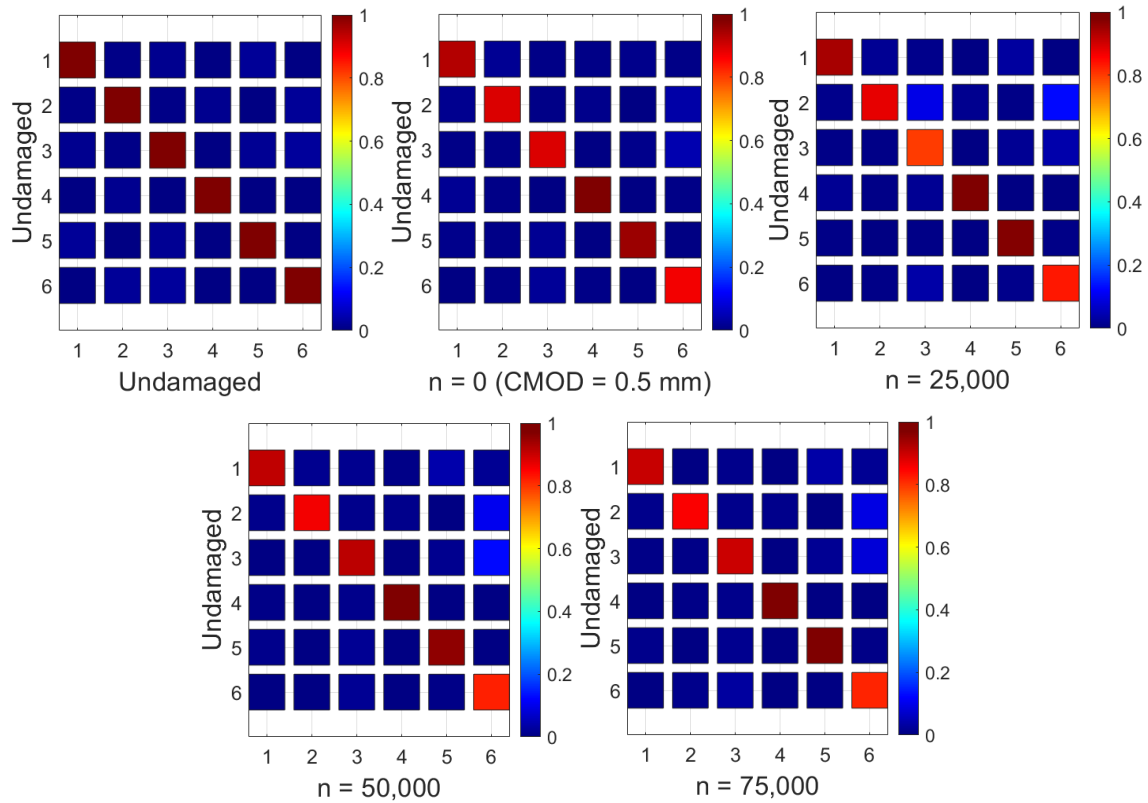


Figure 15: MAC correlation for the undamaged and damaged phases along the fatigue test for specimen 1 (CP1).

The results of the MAC analysis revealed significant changes in MAC values for modes 1, 2, 3 and 6 in the presence of damage. As can be seen in Figure 15, even with damage, all modes are correlated to each other (higher than 80%). These results shown that the beams maintain the dynamic behavior during the cyclic loading.

Damage is often a localized phenomenon, and it is better captured by higher frequency modes. In contrast, lower frequency modes tend to represent the global response and are less sensitive to localized changes [21]. The first mode showed a subtle sensibility to damage in MAC. however, were the most sensitive to frequency variation. This sensitivity is even lower for modes 4 and 5. These modes were also insensitive to damage. As damage increases, the corresponding MAC value should decrease accordingly. However, an important observation is that the MAC value declined at cycle 25000 but increased afterward. This sudden increase in MAC value could be attributed to the complexities involved in obtaining accurate modes during the modal test, possibly influencing the correlation analysis. As can be seen in Figure 16, this decrease in MAC does not occur for the other samples.

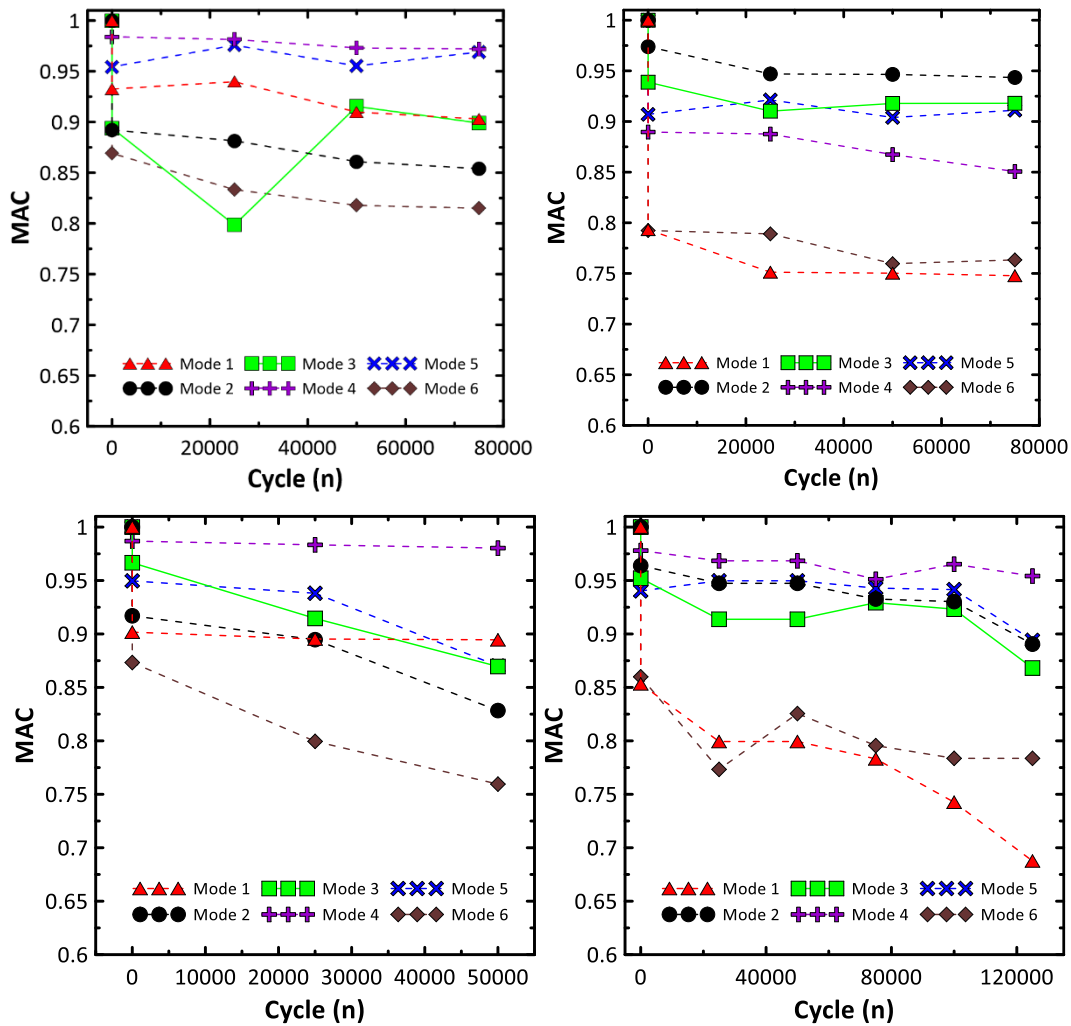


Figure 16: MAC values for the undamaged and damaged phases along the fatigue test for specimen 1 (CP1), specimen 2 (CP2), specimen 3 (CP3) and specimen 5 (CP5), respectively.

Overall, the MAC analysis provides valuable insights into the correlation between undamaged and damaged modes, offering a tool for assessing structural changes caused by fatigue-induced damage to the global behavior of the material in the presence of damage.

4.2.3 Damage identification using damping ratios

Compared to natural frequencies and mode shapes, the application of damping for structural damage identification has been relatively less frequent. This is mainly due to the challenges associated with traditional damping measurement techniques and the complexity of its underlying mechanism. However, advancements in vibration sensors

and post-processing software have made it feasible to acquire dynamic responses accurately, making damping measurements more convenient. Past research has provided valuable insights into using damping as an efficient dynamic feature for detecting, locating, and quantifying damage [15]. The results of damping ratios and their evolution are presented in Table 8 for specimen 1 (CP1), highlighting the material's energy dissipation and its variations with increasing damage during fatigue. $\Delta Damping$ denote the difference of damage ($Damping_0 - Damping_d$) at damage state d . Damage state $d = 0$ correspond to the undamaged state.

Table 8: Identified experimental damping ratios for all stages and its evolution for specimen 1 (CP1).

Modal Shape		M1	M2	M3	M4	M5	M6
Undamaged	Damping	2.706	1.298	0.472	0.439	0.462	0.444
n = 0 (CMOD = 0.5 mm)	Damping	6.092	3.001	1.993	0.634	0.504	0.421
	$\Delta Damping$	125%	131%	322%	44%	9%	-5%
n = 25,000	Damping	6.119	3.575	1.98	0.666	0.5	1.097
	$\Delta Damping$	126%	175%	319%	52%	8%	147%
n = 50,000	Damping	4.492	3.661	1.228	0.657	0.543	0.899
	$\Delta Damping$	66%	182%	160%	50%	18%	102%
n = 75,000	Damping	3.007	2.231	1.738	0.65	0.519	0.518
	$\Delta Damping$	11%	72%	268%	48%	12%	17%

Figure 18.a illustrates the evolution of the material's energy absorption capacity from an undamaged state, relative to the elastic part of the force-displacement curve, to a damaged state with a CMOD of 0.5 mm for the specimen 1 (CP1). As the material transitions to a cracked state, its energy absorption capacity increases, indicating increased ductility. Similarly, the damping ratio is associated with the dissipation of mechanical energy, with energy dissipation (E_{diss}) corresponding to the work done by the damping force in a unit volume of the material in the adapted equations Eq. 4 and Eq. 5 in accordance with Monteiro [44] and Cerqueira [45] expresses the energy absorption capacity at each cycle K .

$$E_{diss,i} = \oint P(CMOD)dCMOD \quad (4)$$

$$EAC_K = \int_{i=1}^N E_{diss,i}(n)dn - \int_{i=1}^K E_{diss,i}(n)dn \quad (5)$$

Where $E_{diss,i}$ is the energy released at each loading cycle i , P is the applied load and EAC is associated to the total energy absorption capacity after K cycles.

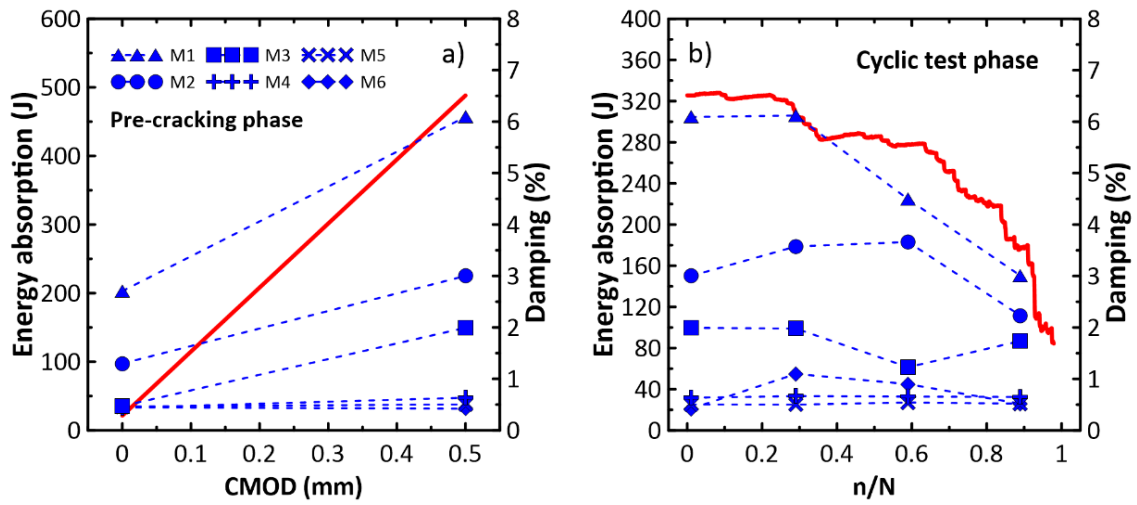


Figure 18: Energy absorption (a) and absorption versus damping (b) over the fatigue test for specimen 1 (CP1).

The energy absorption capacity shows lower value corresponding to the undamaged phase, followed by an abrupt increase after pre-cracking. Figure 18.b displays the damping evolution, showing a pattern closely related to mechanical energy dissipation [51]. The first mode (flexural mode) exhibits a similar trend in energy absorption capacity, showing to be more representative to the global mechanical behavior. In the undamaged phase, the material demonstrates lower damping, which increases by 125% and eventually decreases by 50% in comparison of the first cycle. For the second mode (first torsional mode), damping increases after the undamaged phase and remains constant throughout subsequent cycles. For the other modes, there is no significant variation along the fatigue life.

Figure 19.a provides an overview of the variation in damping for the first flexural mode and the energy absorption capacity for all specimens, comparing both the uncracked and the cracked states with a 0.5 mm CMOD. Meanwhile, Figure 19.b and Figure 19.c shows the dynamic changes in energy absorption capacity and damping ratios, respectively, throughout the fatigue life.

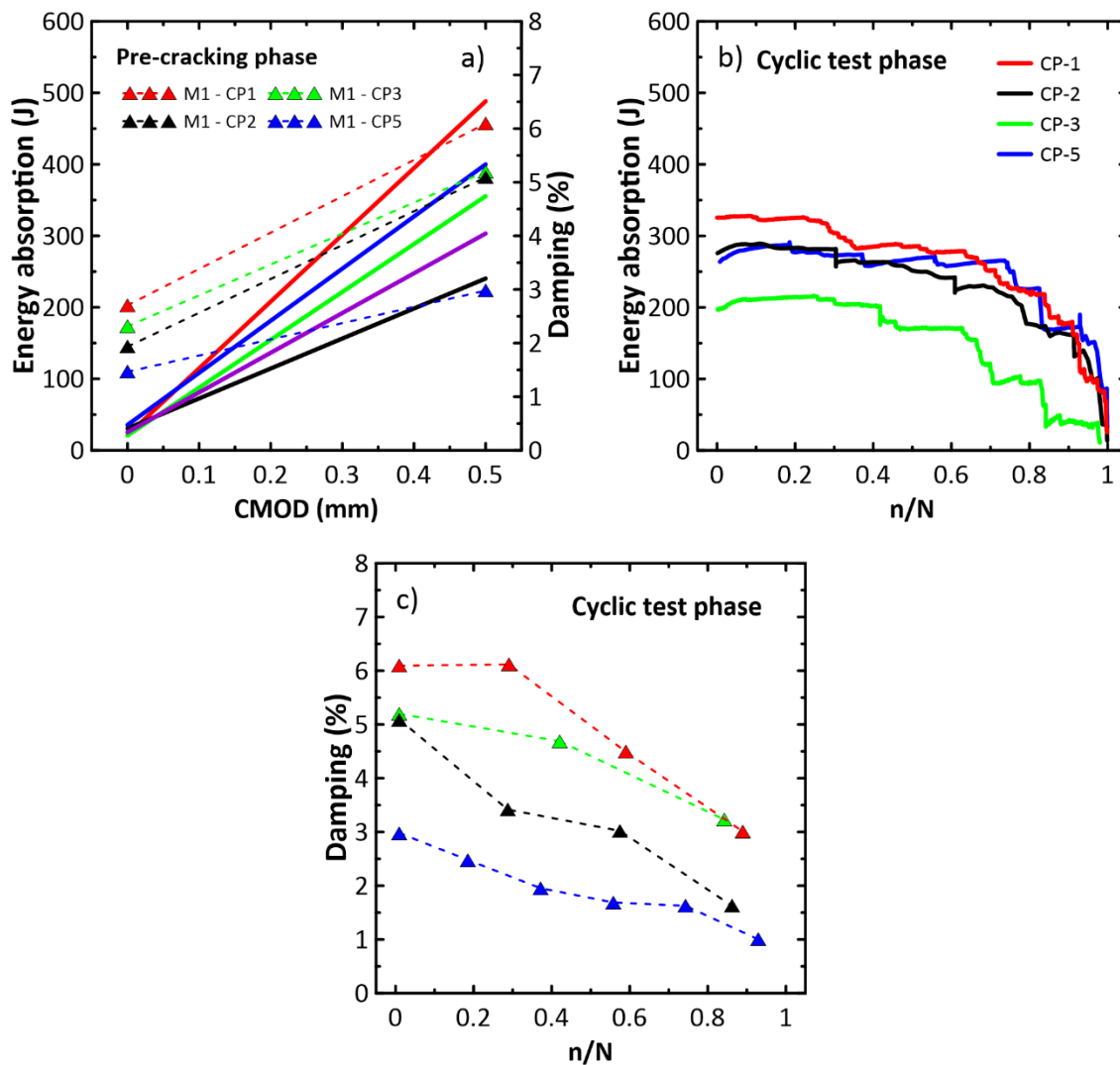


Figure 19: Evolution of the mechanical and modal parameters for the first flexural mode. Energy absorption capacity and damping variation for the uncracked state and after the pre-cracking stage (a), decrease of energy absorption capacity (b) evolution of damping during the fatigue life (c).

Throughout the fatigue life, a pattern appears. Initially, during the early cycles, there is an apparent reduction in variability of damping ratios. Subsequently, a gradual decrease is observed, continuing until approximately 90% of the fatigue life has been reached. Beyond this point, the damping ratios tend to approach a critical level that follows to material failure.

Some studies have reported that damping has the potential to characterize damage more precisely than natural frequencies and mode shapes [52,53]. However, damping has a higher variance in its estimation than frequency [52] as shown in Table 8 of this work and therefore not as reliable.

To represent damping accurately, equivalent damping ratios associated with each eigenmode are utilized, assuming negligible coupling between modes. In the initial uncracked state, characterized by low stress intensity, the observed damping ratios are relatively low. However, once pre-cracking occurs, a significant increase in the damping ratios is shown. The equivalent damping ratio is stress intensity-dependent and increases with the formation of cracks, reaching relatively high values in the final cracked state compared to the initial uncracked state, possibly two or three times higher.

According with Bachmann [46], this amplified damping ratios happens in reinforced concrete by resulting from both viscous damping and friction damping mechanisms. It is important to mention that the Artemis software [50] do not consider the friction damping, using only viscous damping in the analysis. In the uncracked state, the concrete primarily exhibits viscous damping, while the cracked state introduces both viscous and friction damping due to the interactions between the concrete matrix and the reinforcement rebars in the cracked tension zone. Particularly, the interaction between the concrete matrix and the fiber reinforcement in the cracked tension zone must create a similar interaction influencing these damping characteristics.

5 Conclusions

This study presents a methodology for characterizing the modal parameters and damage identification of steel fiber reinforced concrete subjected to fatigue loading and their evolution throughout the cycles. First, the fatigue mechanical deterioration along the cycles was characterized based on previously developed fatigue tests in pre-cracked specimens. Through the impact hammer test, the dynamic properties (frequency, damping ratios, and vibration modes) were first characterized on undamaged and pre-crack specimens. Thereafter, the non-destructive test was carried out along the fatigue cycles to study the correlation between the FRC dynamic properties and its main mechanical variables. The main contribution of this research is to propose key correlations between the main mechanical and dynamical parameters and bring a new methodology to verify damage through non-destructive tests. The following conclusions were derived from present research:

- The mechanical degradation was mainly analyzed in accordance with the crack mouth opening displacement (CMOD) evolution, stiffness decay and energy release evolution along the cycles. It was shown that the CMOD evolution for

all specimens presented a stable increase in crack opening at a decreasing rate of CMOD, followed by a slow and gradual increase in CMOD in a linear manner per cycle, and finally a rapid increase in crack opening and a drastic decrease of stiffness until total rupture of the material. For the loading and unloading steps it showed a slight increase in CMOD what could shorten the fatigue life. After pre-cracking, the stiffness presented a great drop and during the fatigue test, the stiffness presents an S-shaped curve, that is characterized by an initial deceleration stage followed by an almost linear second phase. When the specimen reaches its failure, the last stage of stiffness degradation is a sharp decrease.

- The energy imparted to test allowed the identification of six vibration modes varying from 923.12 Hz to 5736.43 Hz, this frequency range was enough to identify six vibration modes predominated by flexural and torsional behavior. The reduction in stiffness caused a decrease in the frequency of the material by up to 54% for the first flexural mode and 44% for the first torsional mode at the end of the fatigue life.
- Moreover, the MAC was used for damage identification as an index to analyze the sensitivity of damage in mode shapes. Thus, the MAC analysis was able to identify the modes with presence of damage and the modes 1,2, 3 and 6 showed to be more affected. Showing that not only the first modes have influence in global behavior of the material, but also the higher modes.
- For damping ratios, the first and second modes (flexional and torsional mode, respectively) were more significant to analyze the variation of damage. The first flexural mode showed to be more representative with the mechanical evolution of the material for both frequency and damping variation along the fatigue. Therefore, this analysis highlights the intrinsic relationship between the cracking state, damping behavior, and energy absorption capacity of the specimens. The findings demonstrate the pronounced effects of pre-cracking on the damping properties, which showed a greater coefficient of variation value than frequency during the cracked state for damage identification. This could potentially have implications for the overall structural performance and durability of the materials under cyclic loading conditions.

6 Acknowledgements

All testing was conducted at the Laboratory of Structures and Materials of the Pontifical Catholic University of Rio de Janeiro. This study was financed in part by the Coordenação de Aperfeiçoamento de Pessoal de Nível Superior - Brasil (CAPES) - Finance code 001. This research is part of the cooperation project Aneel PD-0394-1905/2019 (Furnas - PUC-Rio). For more details about the project, please assess www.fadiga.civ.puc-rio.br.

References

- [1] Lee MK, Barr BIG. An overview of the fatigue behaviour of plain and fibre reinforced concrete. *Cem Concr Compos* 2004;26:299–305. [https://doi.org/10.1016/S0958-9465\(02\)00139-7](https://doi.org/10.1016/S0958-9465(02)00139-7).
- [2] Destebeccq J-F. *Cyclic and Dynamic Loading Fatigue of Structural Concrete*. Mech. Behav. Concr., Hoboken, NJ USA: John Wiley & Sons, Inc.; 2013, p. 185–224. <https://doi.org/10.1002/9781118557587.ch5>.
- [3] Zhang B, Phillips D V., Wu K. Effects of loading frequency and stress reversal on fatigue life of plain concrete. *Mag Concr Res* 1996;48:361–75. <https://doi.org/10.1680/mac.1996.48.177.361>.
- [4] Abbas S, Nehdi ML, Saleem MA. Ultra-High Performance Concrete: Mechanical Performance, Durability, Sustainability and Implementation Challenges. *Int J Concr Struct Mater* 2016;10:271–95. <https://doi.org/10.1007/s40069-016-0157-4>.
- [5] Xargay H, Ripani M, Folino P, Núñez N, Caggiano A. Acoustic emission and damage evolution in steel fiber-reinforced concrete beams under cyclic loading. *Constr Build Mater* 2021;274. <https://doi.org/10.1016/j.conbuildmat.2020.121831>.
- [6] Sinaie S, Heidarpour A, Zhao XL, Sanjayan JG. Effect of size on the response of cylindrical concrete samples under cyclic loading. *Constr Build Mater* 2015;84:399–408. <https://doi.org/10.1016/j.conbuildmat.2015.03.076>.
- [7] Boulekbache B, Hamrat M, Chemrouk M, Amziane S. Flexural behaviour of steel fibre-reinforced concrete under cyclic loading. *Constr Build Mater* 2016;126:253–62. <https://doi.org/10.1016/j.conbuildmat.2016.09.035>.
- [8] Germano F, Tiberti G, Plizzari G. Post-peak fatigue performance of steel fiber reinforced concrete under flexure. *Mater Struct Constr* 2016;49:4229–45. <https://doi.org/10.1617/s11527-015-0783-3>.
- [9] Makita T, Brühwiler E. Tensile fatigue behaviour of ultra-high performance fibre reinforced concrete (UHPFRC). *Mater Struct Constr* 2014;47:475–91.

<https://doi.org/10.1617/s11527-013-0073-x>.

[10] González DC, Moradillo R, Mínguez J, Martínez JA, Vicente MA. Postcracking residual strengths of fiber-reinforced high-performance concrete after cyclic loading. *Struct Concr* 2018;19:340–51. <https://doi.org/10.1002/suco.201600102>.

[11] Paluri Y, Noolu V, Mudavath H, Kumar Pancharathi R. Flexural Fatigue Behavior of Steel Fiber-Reinforced Reclaimed Asphalt Pavement–Based Concrete: An Experimental Study. *Pract Period Struct Des Constr* 2021;26:1–10. [https://doi.org/10.1061/\(asce\)sc.1943-5576.0000540](https://doi.org/10.1061/(asce)sc.1943-5576.0000540).

[12] Miao B, Chern JC, Yang CA. Influences of fiber content on properties of self-compacting steel fiber reinforced concrete. *J Chinese Inst Eng Trans Chinese Inst Eng A/Chung-Kuo K Ch'eng Hsueh K'an* 2003;26:523–30. <https://doi.org/10.1080/02533839.2003.9670805>.

[13] Li B, Xu L, Chi Y, Huang B, Li C. Experimental investigation on the stress-strain behavior of steel fiber reinforced concrete subjected to uniaxial cyclic compression. *Constr Build Mater* 2017;140:109–18. <https://doi.org/10.1016/j.conbuildmat.2017.02.094>.

[14] Naaman AE, Hammoud H. Fatigue characteristics of high performance fiber-reinforced concrete. *Cem Concr Compos* 1998;20:353–63. [https://doi.org/10.1016/S0958-9465\(98\)00004-3](https://doi.org/10.1016/S0958-9465(98)00004-3).

[15] Ranjbaran F, Rezaifar O, Mirzababai R. Experimental investigation of steel fiber-reinforced concrete beams under cyclic loading. *Int J Adv Struct Eng* 2018;10:49–60. <https://doi.org/10.1007/s40091-018-0177-1>.

[16] Wang B, Gupta R. Performance of Repaired Concrete under Cyclic Flexural Loading. *Materials (Basel)* 2021;14:1363. <https://doi.org/10.3390/ma14061363>.

[17] Simo JC, Ju JW. Strain- and stress-based continuum damage models-I. Formulation. *Int J Solids Struct* 1987;23:821–40. [https://doi.org/10.1016/0020-7683\(87\)90083-7](https://doi.org/10.1016/0020-7683(87)90083-7).

[18] Shan Z, Yu Z, Li X, Xie Y. Damage Quantification in Concrete under Fatigue Loading Using Acoustic Emission. *J Sensors* 2019;2019. <https://doi.org/10.1155/2019/1359853>.

[19] Krahl PA, Gidrão G de MS, Carrazedo R. Cyclic behavior of UHPFRC under compression. *Cem Concr Compos* 2019;104:103363. <https://doi.org/10.1016/j.cemconcomp.2019.103363>.

[20] Alampalli S, Ettouney M. Structural identification, damage identification and

structural health monitoring. *Nondestruct Charact Compos Mater Aerosp Eng Civ Infrastructure, Homel Secur* 2007;2007;6531:65310L. <https://doi.org/10.1117/12.715000>.

[21] Doebling SW, Farrar CR, Prime MB. A summary review of vibration-based damage identification methods. *Shock Vib Dig* 1998;30:91–105. <https://doi.org/10.1177/058310249803000201>.

[22] Farrar CR, Doebling SW, Nix DA. Vibration-based structural damage identification. *Philos Trans R Soc London Ser A Math Phys Eng Sci* 2001;359:131–49. <https://doi.org/10.1098/rsta.2000.0717>.

[23] Dilena M, Limongelli MP, Morassi A. Damage localization in bridges via the FRF interpolation method. *Mech Syst Signal Process* 2015;52–53:162–80. <https://doi.org/10.1016/j.ymssp.2014.08.014>.

[24] Rodrigues Gaspar CM, Nascimento Beserra JH, Taissum Cardoso DC. Non-destructive mechanical characterisation of thin-walled GFRP beams through dynamic testing and model updating. *Compos Part B Eng* 2021;224. <https://doi.org/10.1016/j.compositesb.2021.109212>.

[25] Lee E-T, Hong Y-S, Eun H-C. Prediction of the Physical Properties of a Structural Member by the Impact Hammer Test. *Sensors* 2022;22:6762. <https://doi.org/10.3390/s22186762>.

[26] Cao MS, Sha GG, Gao YF, Ostachowicz W. Structural damage identification using damping: a compendium of uses and features. *Smart Mater Struct* 2017;26:043001. <https://doi.org/10.1088/1361-665X/aa550a>.

[27] Rainieri F. *Operational Modal Analysis of Civil Engineering Structures*. 2014.

[28] Cheynet E, Jakobsena JB, Snæbjörnsson J. Damping estimation of large wind-sensitive structures. *Procedia Eng* 2017;199:2047–53. <https://doi.org/10.1016/j.proeng.2017.09.471>.

[29] Chung DDL. Review: Materials for vibration damping. *J Mater Sci* 2001;36:5733–7. <https://doi.org/10.1023/A:1012999616049>.

[30] Feng D, Feng MQ. Output-only damage detection using vehicle-induced displacement response and mode shape curvature index. *Struct Control Heal Monit* 2016;23:1088–107. <https://doi.org/10.1002/stc.1829>.

[31] Zhao J, Zhang L. Structural Damage Identification Based on the Modal Data Change. *Int J Eng Manuf* 2012;2:59–66. <https://doi.org/10.5815/ijem.2012.04.08>.

[32] Figueiredo TCSP, Gaspar CMR, Hering M, Curosu I, Curbach M, Mechtcherine

V, et al. Experimental modal analysis of RC beams strengthened with SHCC subjected to shear under impact strain rates. *Eng Struct* 2022;264. <https://doi.org/10.1016/j.engstruct.2022.114459>.

[33] Frizzarin M, Feng MQ, Franchetti P, Soyoz S, Modena C. Damage detection based on damping analysis of ambient vibration data. *Struct Control Heal Monit* 2008;n/a-n/a. <https://doi.org/10.1002/stc.296>.

[34] Carne TG, James GH. The inception of OMA in the development of modal testing technology for wind turbines. *Mech Syst Signal Process* 2010;24:1213–26. <https://doi.org/10.1016/j.ymsp.2010.03.006>.

[35] Cawley P, Adams RD. The Location of Defects in Structures From Measurements of Natural Frequencies *The Journal of Strain Analysis for Engineering Design. J Strain Anal Eng Des* 1979;14:49–57.

[36] Salawu OS. Detection of structural damage through changes in frequency: A review. *Eng Struct* 1997;19:718–23. [https://doi.org/10.1016/S0141-0296\(96\)00149-6](https://doi.org/10.1016/S0141-0296(96)00149-6).

[37] Dilella M, Morassi A. Dynamic testing of a damaged bridge. *Mech Syst Signal Process* 2011;25:1485–507. <https://doi.org/10.1016/j.ymsp.2010.12.017>.

[38] Method ST, Flow S, Concrete S. WSDOT FOP for ASTM C 1611 Standard Test Method for Slump Flow of Self-Consolidating Concrete 2017:1–6.

[39] BIBM, CEMBUREAU, ERMCO, EFCA E. The European Guidelines for Self-Compacting Concrete. *Eur Guidel Self Compact Concr* 2005:63.

[40] Cardoso DCT, Pereira GBS, Silva FA, Silva Filho JJH, Pereira E V. Influence of steel fibers on the flexural behavior of RC beams with low reinforcing ratios: Analytical and experimental investigation. *Compos Struct* 2019;222:110926. <https://doi.org/10.1016/j.compstruct.2019.110926>.

[41] European Standards. Test method for metallic fibered concrete - Measuring the flexural tensile strength (limit of proportionality (LOP), residual). *Eur Stand CEN* 2005:1–17.

[42] Brandt A. Noise and vibration analysis and control: signal analysis and experimental procedures. 2010.

[43] Carlesso DM, de la Fuente A, Cavalaro SHP. Fatigue of cracked high performance fiber reinforced concrete subjected to bending. *Constr Build Mater* 2019;220:444–55. <https://doi.org/10.1016/j.conbuildmat.2019.06.038>.

[44] Moreira de Alencar Monteiro V, Carlos Taissum Cardoso D, de Andrade Silva F. A novel methodology for estimating damage evolution and energy dissipation for steel

fiber reinforced concrete under flexural fatigue loading. *Int J Fatigue* 2023;166:107244. <https://doi.org/10.1016/j.ijfatigue.2022.107244>.

[45] Cerqueira NR de A, Monteiro VM de A, de Souza FR, Cardoso DCT, Silva F de A. Mechanical degradation of ultra-high performance concrete under flexural fatigue loading. *Constr Build Mater* 2023;391. <https://doi.org/10.1016/j.conbuildmat.2023.131877>.

[46] Bachmann H, Ammann WJ, Deischl F, Eisenmann J, Floegl I, Hirsch GH, et al. *Vibration Problems in Structures*. Basel: Birkhäuser Basel; 1995. <https://doi.org/10.1007/978-3-0348-9231-5>.

[47] Newman J, Ruschau JJ. The stress-level effect on fatigue-crack growth under constant-amplitude loading. *Int J Fatigue* 2007;29:1608–15. <https://doi.org/10.1016/j.ijfatigue.2006.11.003>.

[48] Keerthana K, Kishen JMC. Micromechanical Effects of Loading Frequency on Fatigue Fracture in Concrete. *J Eng Mech* 2021;147:1–11. [https://doi.org/10.1061/\(ASCE\)EM.1943-7889.0002018](https://doi.org/10.1061/(ASCE)EM.1943-7889.0002018).

[49] Castillo E, Canteli AF. *A unified statistical methodology for modelling fatigue damage*. 2009.

[50] ARTEMIS MODAL. *Structure Vibration and Solutions A/S*. Version 7.1.0.6, 2021.

[51] H.Abdul Razak, F.C Choi. The effect of corrosion on the natural frequency and modal damping of reinforced concrete beams. *Engineering Structures*, 2001; Volume 23, Issue 9, Pages 1126-1133. [https://doi.org/10.1016/S0141-0296\(01\)00005-0](https://doi.org/10.1016/S0141-0296(01)00005-0).

[52] Modena C, Sonda D, Zonta D. Damage Localization in Reinforced Concrete Structures by Using Damping Measurements. *Key Eng Mater* 1999;167–168:132–41. <https://doi.org/10.4028/www.scientific.net/KEM.167-168.132>.

[53] Yam LH, Wei Z, Cheng L. Nondestructive Detection of Internal Delamination by Vibration-based Method for Composite Plates. *J Compos Mater* 2004;38:2183–98. <https://doi.org/10.1177/0021998304045590>.

[54] Limongelli, Maria Pina et al. *Vibration response-based damage detection. Structural Health Monitoring Damage Detection Systems for Aerospace*, v. 133, 2021.

[55] Brincker, Rune et al. *Damage detection in laboratory concrete beams*. 1994.